Multifunctional bridged-carbon scaffold: a universal electrodeposition platform for bifunctional catalysts toward flexible zinc–air batteries

Jiahui Wang[a,#], Wenhua Shi[a,#], Xiangjun Zheng[a,*], Yaman Cui[a], Jiayu Zhao[a], Xingmei Guo[a], Qianqian Fan[a], Zhongyao Duan[a], Kai Zeng[b,c,*], Junhao Zhang[a,*]

Address

[a] *School of Environmental and Chemical Engineering, Jiangsu University of Science and Technology, Zhenjiang, Jiangsu 212003, China*

[b] *School of Electrical Engineering, Institute of Smart City and Intelligent Transportation, Southwest Jiaotong University, Chengdu 610032, China*

[c] *School of Chemistry and Chemical Engineering, Nanjing University, Nanjing 210023, China*

[#] *These authors contribute equally to this work.*

***Corresponding Author**

E-mail address: zhengxj@just.edu.cn (X. Zheng), zengkai@swjtu.edu.cn (K. Zeng), jhzhang6@just.edu.cn (J. Zhang)

1. Experimental Section

1.1 Chemical Reagents

Thiourea (CH_4N_2S, AR grade), nickel(II) sulfate heptahydrate ($NiSO_4·7H_2O$, AR grade), iron(III) nitrate nonahydrate ($Fe(NO_3)_3·9H_2O$, AR grade), cobalt(II) nitrate hexahydrate ($Co(NO_3)_2·6H_2O$, AR grade), potassium hydroxide (KOH, GR grade), and platinum carbon (Pt/C, 20 wt%) were sourced from Aladdin Biochemical Technology Co., Ltd. Nafion ($C_{10}H_8O$, 5 wt%) was procured from DuPont (USA). Absolute ethanol (C_2H_6O, AR grade), zinc acetate ($Zn(CH_3COO)_2$, AR grade), and acetylene black were obtained from Sinopharm Chemical Reagent Co., Ltd. (China).

1.2 Material Preparation

Synthesis of NS-CCC: A cotton cloth (CC, 5×5 cm^2) was immersed in 10 mL deionized water containing 0.4 g thiourea for 1 h. After drying at 80 °C for 12 h, the thiourea-impregnated CC precursor was carbonized under N_2 atmosphere at 1000 °C (heating rate: 10 °C min^{-1}) for 2 h. The resulting N/S-co-doped cotton carbon cloth was designated as (NS-CCC).

Synthesis of NiFe-LDH/NS-CCC: Electrodeposition was performed using NS-CCC strips (1×2 cm^2) as working electrodes, with Hg/HgO and carbon rod serving as reference and counter electrodes, respectively. The electrolyte was prepared by homogeneously mixing aqueous solutions of 0.015 mol L^{-1} $NiSO_4·7H_2O$ and 0.015 mol L^{-1} $Fe(NO_3)_3·9H_2O$. Constant potential deposition at −1.5 V for 240 s was conducted using a DH7002A workstation (Donghua Instrument Co., China). The electrode was then rinsed with deionized water and vacuum-dried to obtain the NiFe-layered double hydroxide (LDH)/NS-CCC composite.

Synthesis of $Co(OH)_2$/NS-CCC: The procedure matched that of NiFe-LDH/NS-CCC synthesis, with the exception that the electrolyte contained 0.1 mol L^{-1} $Co(NO_3)_2·6H_2O$. Deposition was performed at −1.5 V for 180 s. The final product was designated $Co(OH)_2$/NS-CCC.

Synthesis of FeS/Fe_3O_4/NS-CCC: The standard electrodeposition protocol was followed, except that the electrolyte comprised 0.005 mol L^{-1} $Fe(NO_3)_3·9H_2O$ and 0.5 mol L^{-1} CH_4N_2S. Deposition at −1.5 V for 600 s yielded the FeS/Fe_3O_4/NS-CCC composite.

1.3 Physical Characterization

The compositional profiles of the catalysts were analyzed by X-ray diffraction (XRD; Cu Kα radiation, Bruker D8) and Raman spectroscopy (LabRAM HR 800, 633 nm excitation laser). Morphological and structural characteristics of the samples were characterized through scanning electron microscopy (SEM, QUANTA 250 FEG), high-resolution transmission electron microscopy (HRTEM; FEI Tecnai-G2 F20), and corresponding selected-area electron diffraction (SAED) and scanning transmission electron microscopy (STEM) analyses. Additionally, X-ray photoelectron spectroscopy (XPS; Al Kα radiation, VG ESCALAB MKII) was employed to investigate elemental chemical environments and binding energies.

1.4 Electrocatalytic Performance Evaluation

Electrochemical measurements for oxygen reduction reaction (ORR) and oxygen evolution reaction (OER) activities were performed using a three-electrode configuration (RRDE-3A, Japan) and a CHI 760E electrochemical workstation (Chenhua Instruments, Shanghai). A glassy carbon electrode, carbon rod, and Hg/HgO electrode served as the working, counter, and reference electrodes, respectively, with a catalyst loading of 0.4 mg cm^{-2}. Linear sweep voltammetry (LSV) was performed at 5 mV s^{-1} with 95% *iR* compensation, while cyclic voltammetry (CV) was conducted at 50 mV s^{-1}. Electrochemical impedance spectroscopy (EIS) measurements covered frequencies from 10^6 to 0.01 Hz at OER potentials corresponding to 10 mA cm^{-2}. Catalyst stability was evaluated through accelerated degradation testing (ADT) and chronoamperometry (CA). All measured potentials (vs. Hg/HgO) were converted to the reversible hydrogen electrode (RHE) scale using: $E_{(RHE)} = E_{(Hg/HgO)} + 0.059 \times pH + 0.198$.

1.5 Zinc-Air Battery Assembly and Testing

Flexible ZABs: Zinc foil was utilized as the anode and flexible NiFe-LDH/NS-CCC self-supporting electrodes directly served as air cathodes, with polyacrylic acid (PAA)-based gel polymer electrolyte (GPE) as the electrolyte. Commercial catalysts (Pt/C and RuO_2) were similarly formulated into inks and coated onto carbon cloth for comparison. Both liquid and flexible ZABs were evaluated using a CHI 760E electrochemical workstation and a LAND battery testing system (CT2001A).

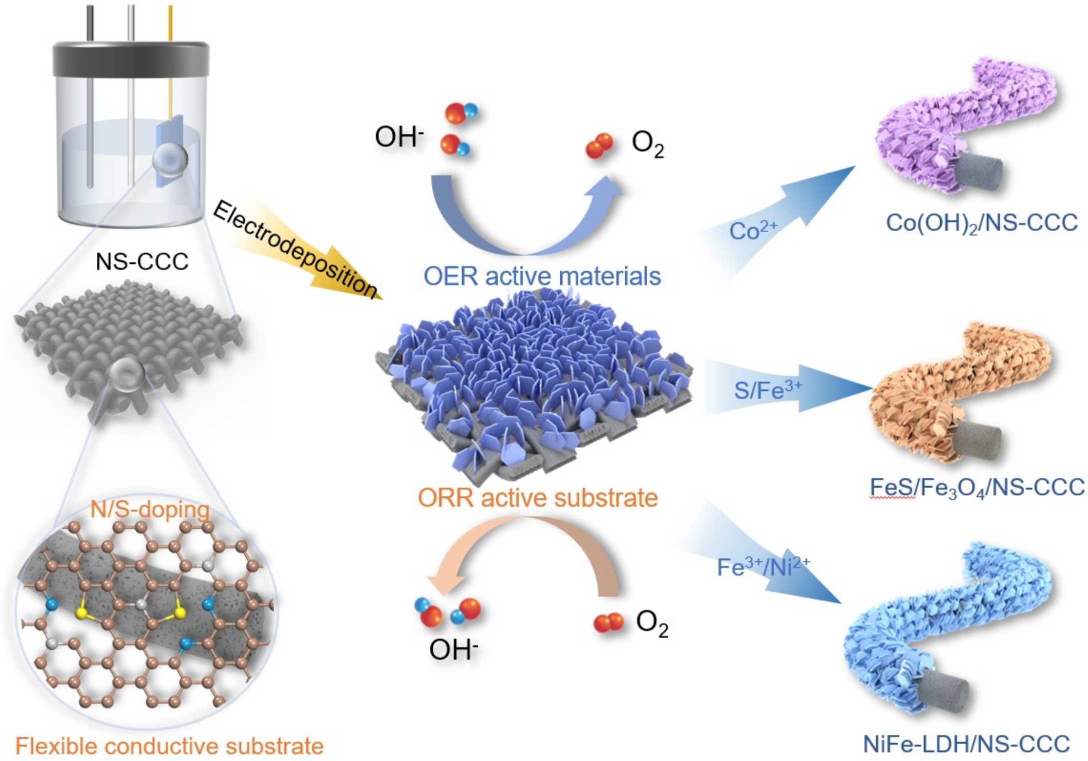

Fig. S1. Schematic diagram depicting the electrodeposition of diverse OER-active materials using NS-CCC as a general flexible substrate.

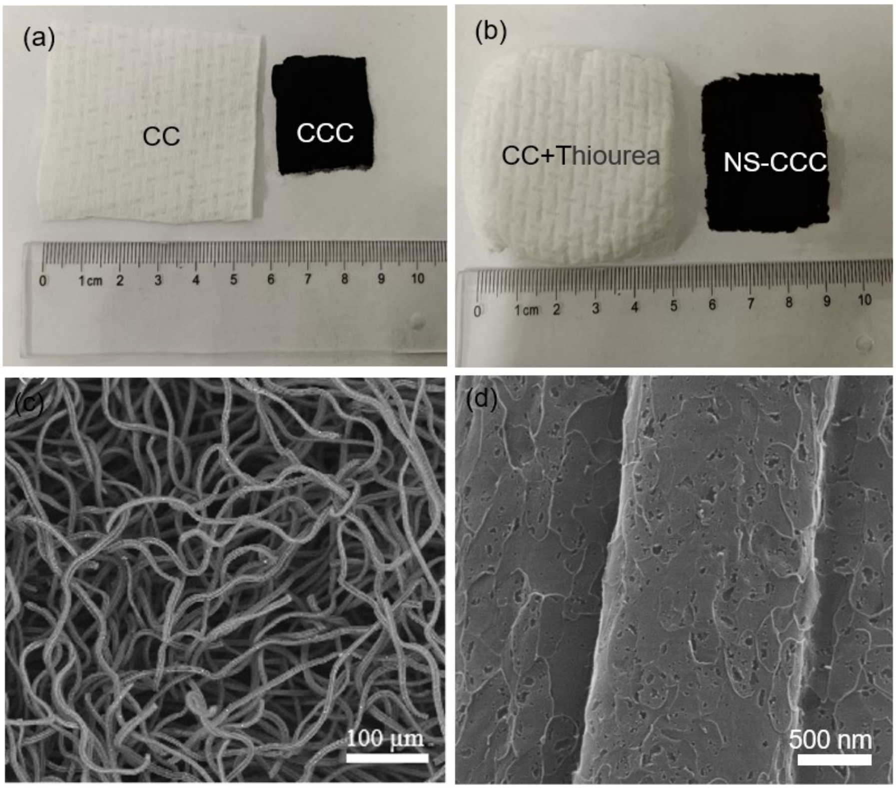

Fig. S2. Photographs of CCC and NS-CCC, SEM images of NS-CCC.

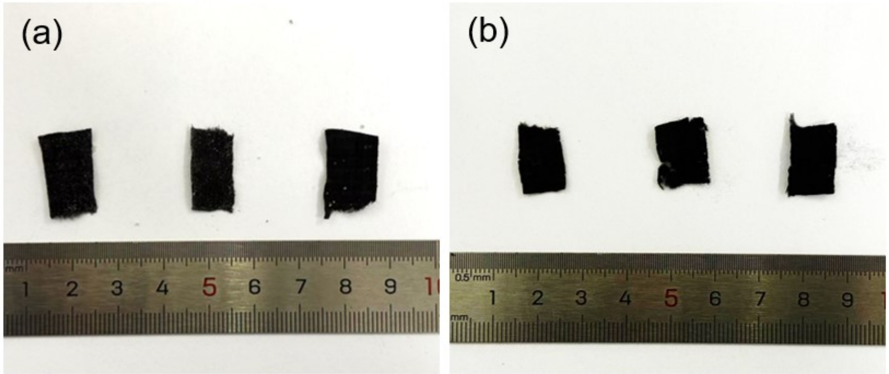

Fig. S3 Photographs of (a) NS-CCC and electrodeposited (b) $Co(OH)_2$/NS-CCC, FeS/Fe_3O_4/NS-CCC, and NiFe-LDH/NS-CCC.

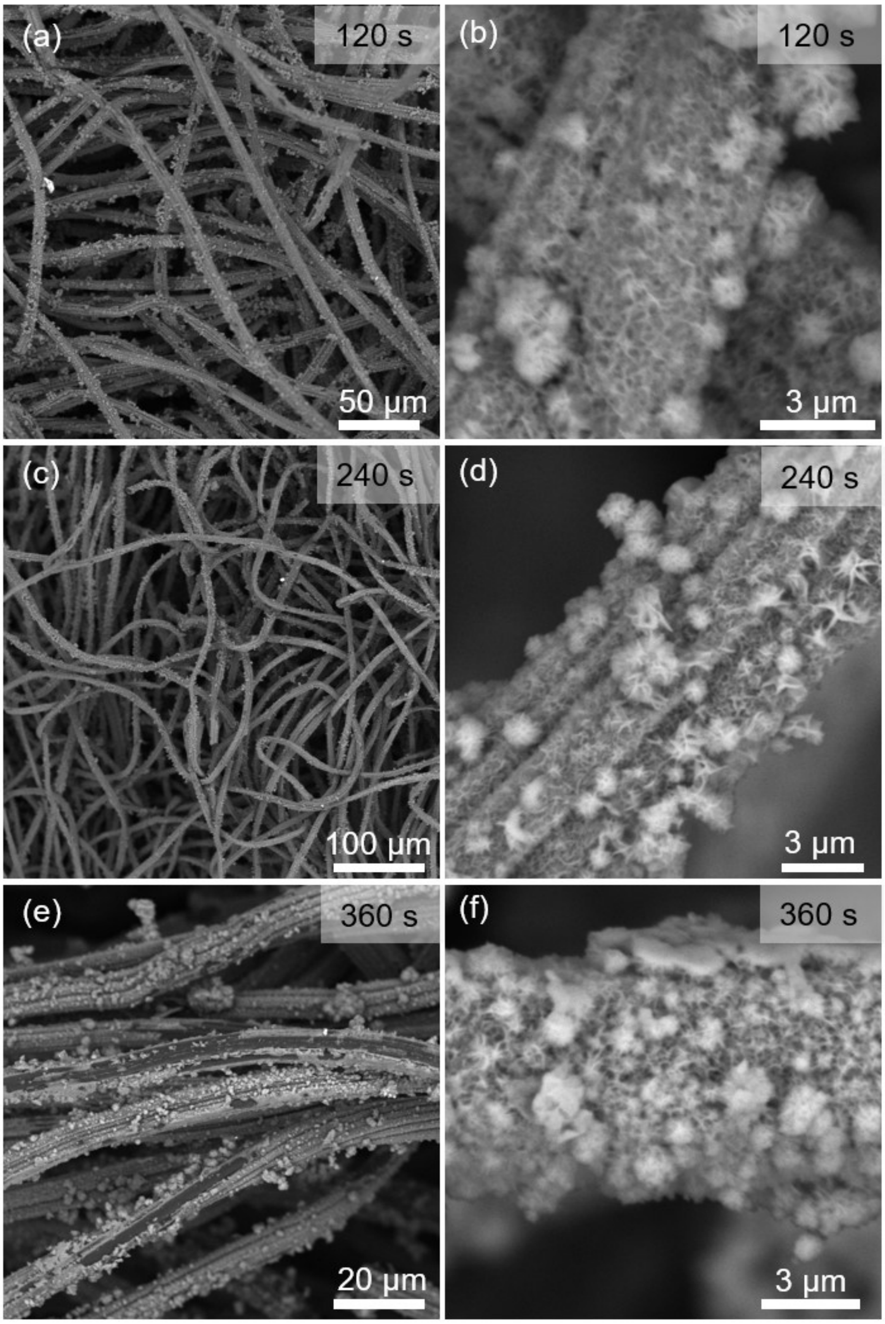

Fig. S4. SEM images of NiFe-LDH/NS-CCC with different electrodeposition times.

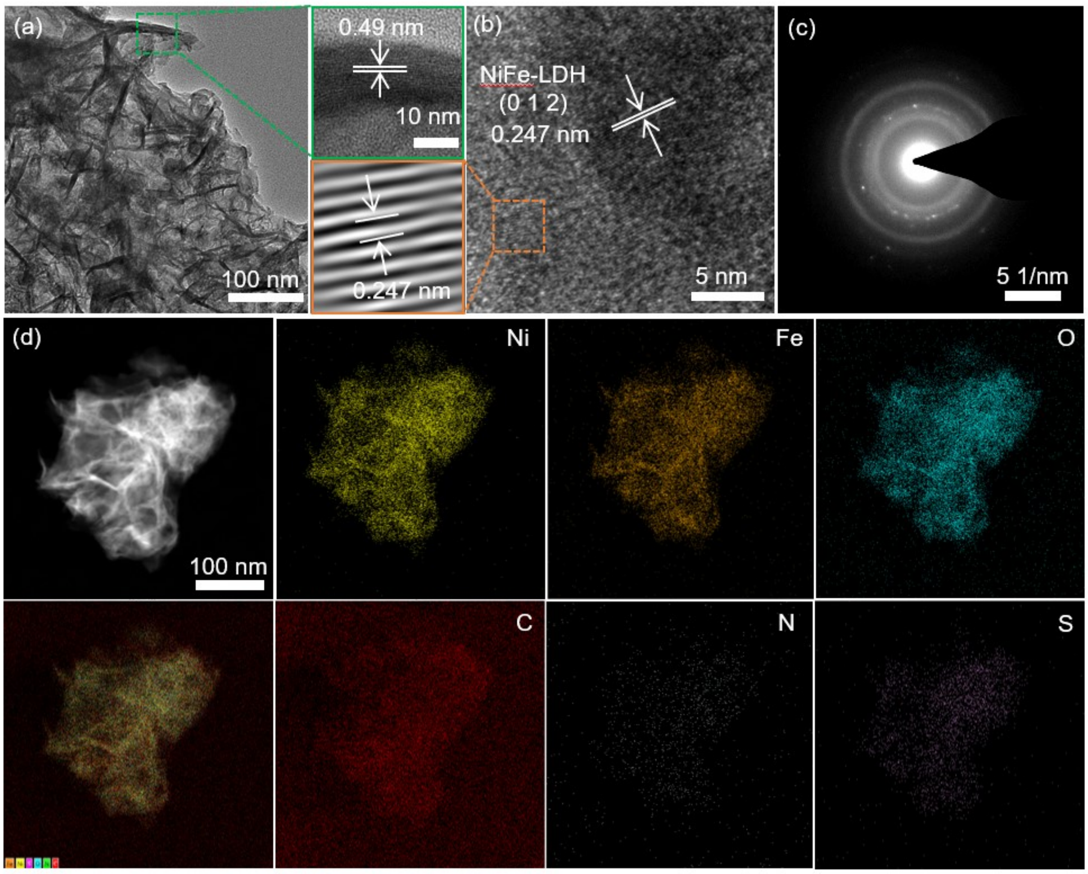

Fig. S5. (a) TEM, (b) HRTEM images, (c) SEAD pattern, and (d) STEM image and the corresponding elemental mappings of NiFe-LDH/NS-CCC.

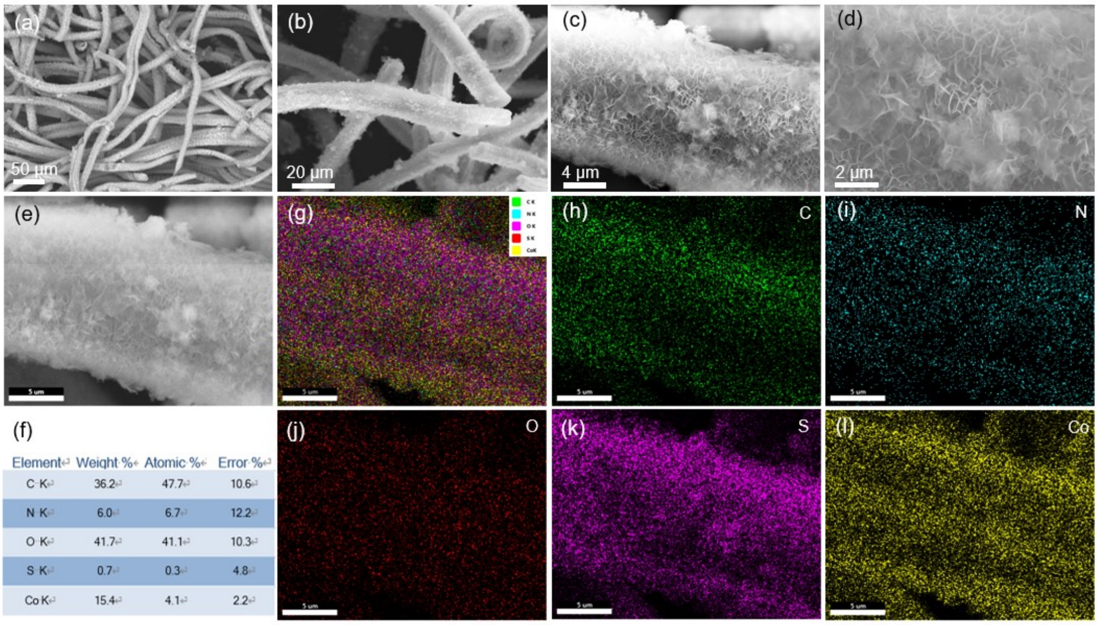

Fig. S6. (a-d) SEM, (e-f) EDS, and (g-l) element mapping images of $Co(OH)_2$/NS-CCC.

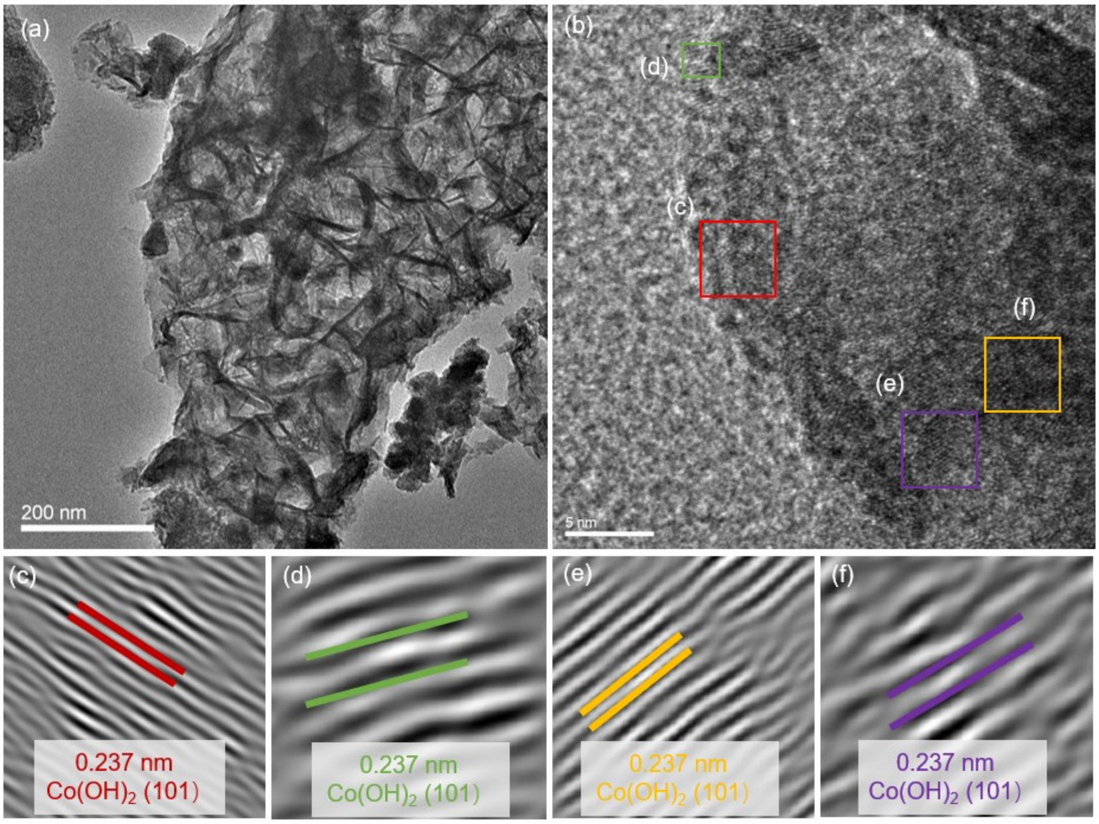

Fig. S7. (a,b) TEM and (c-f) FFT images of $Co(OH)_2$/NS-CCC.

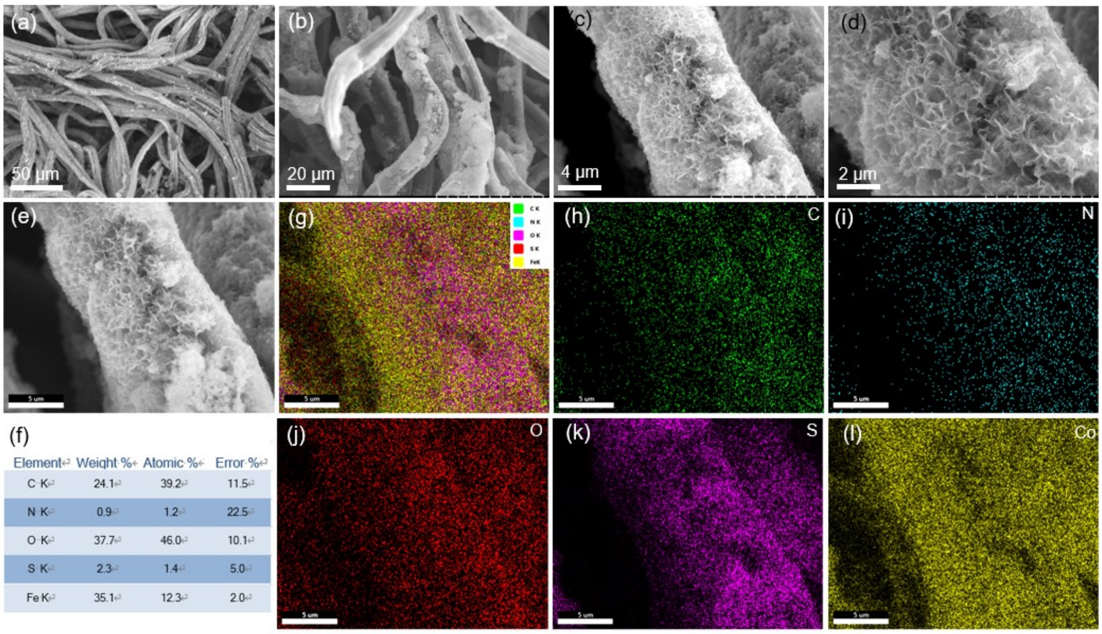

Element	Weight %	Atomic %	Error %
C K	24.1	39.2	11.5
N K	0.9	1.2	22.5
O K	37.7	46.0	10.1
S K	2.3	1.4	5.0
Fe K	35.1	12.3	2.0

Fig. S8. (a-d) SEM, (e-f) EDS, and (g-l) element mapping images of FeS/Fe_3O_4/NS-CCC.

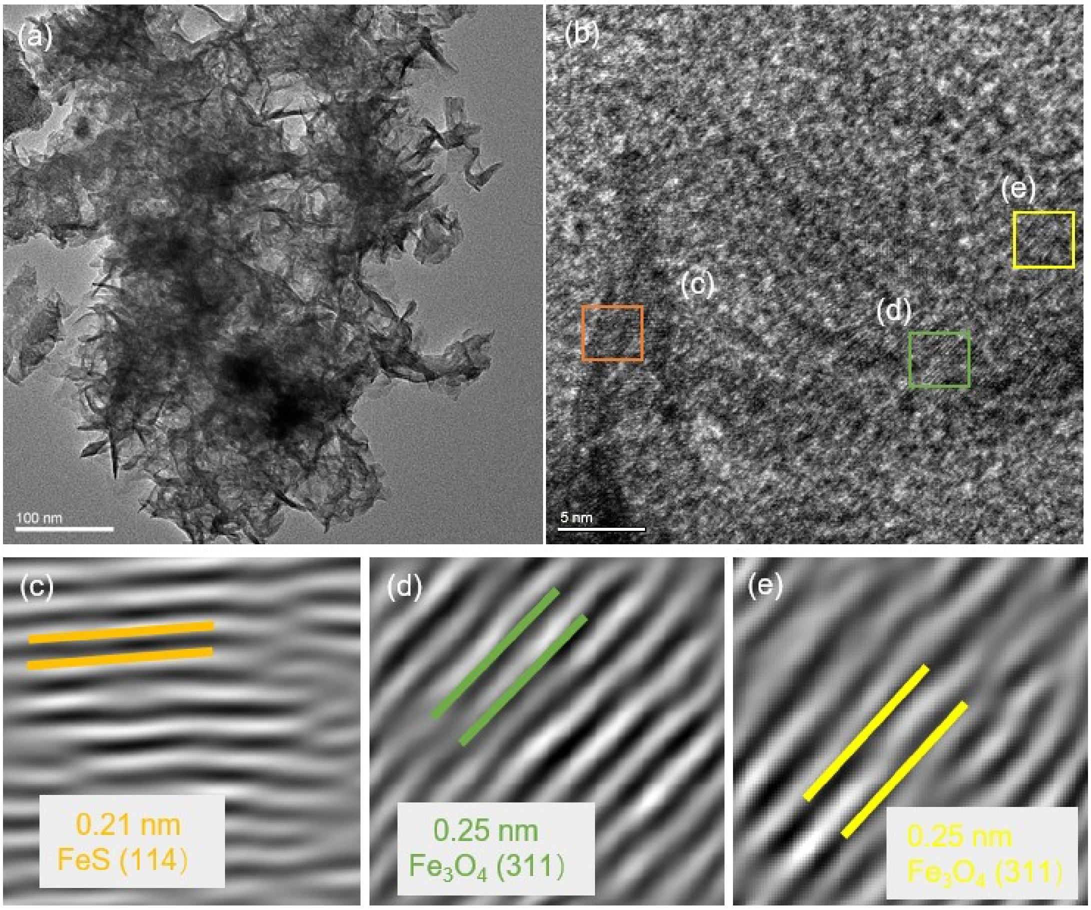

Fig. S9. (a,b) TEM and (c-e) FFT images of FeS/Fe_3O_4/NS-CCC.

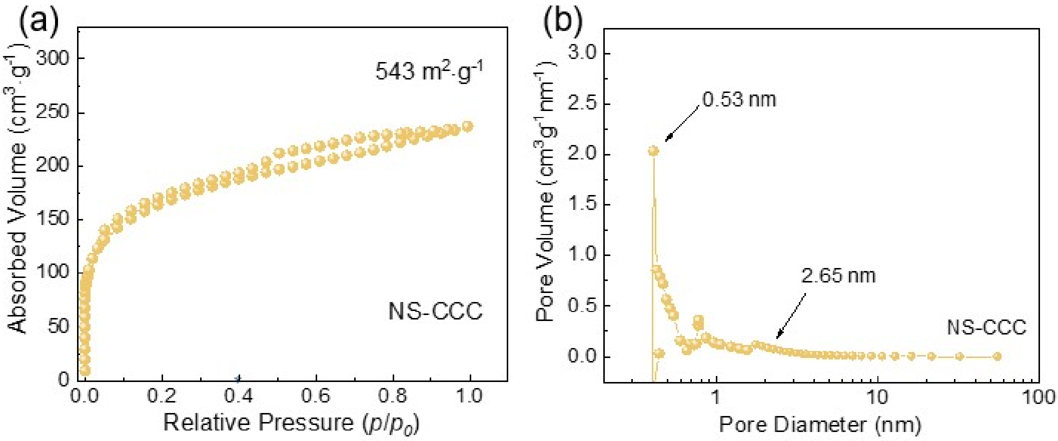

Fig. S10. (a) N_2 adsorption-desorption isotherms, (b) Pore size distribution profile of the NS-CCC substrate.

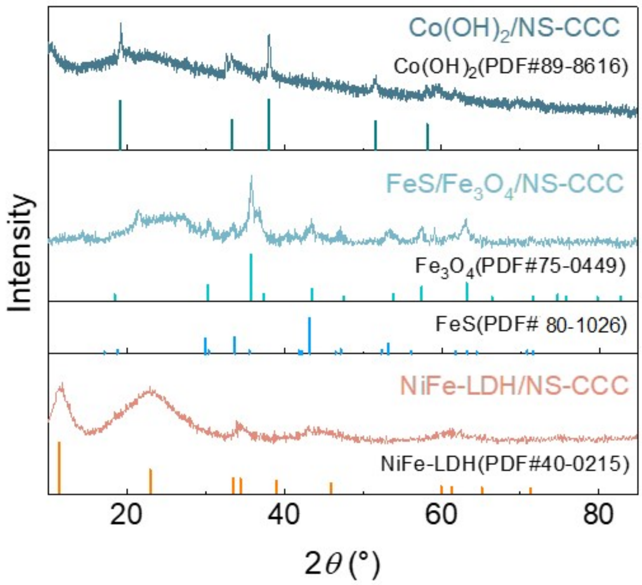

Fig. S11. XRD patterns with PDF cards of the prepared samples.

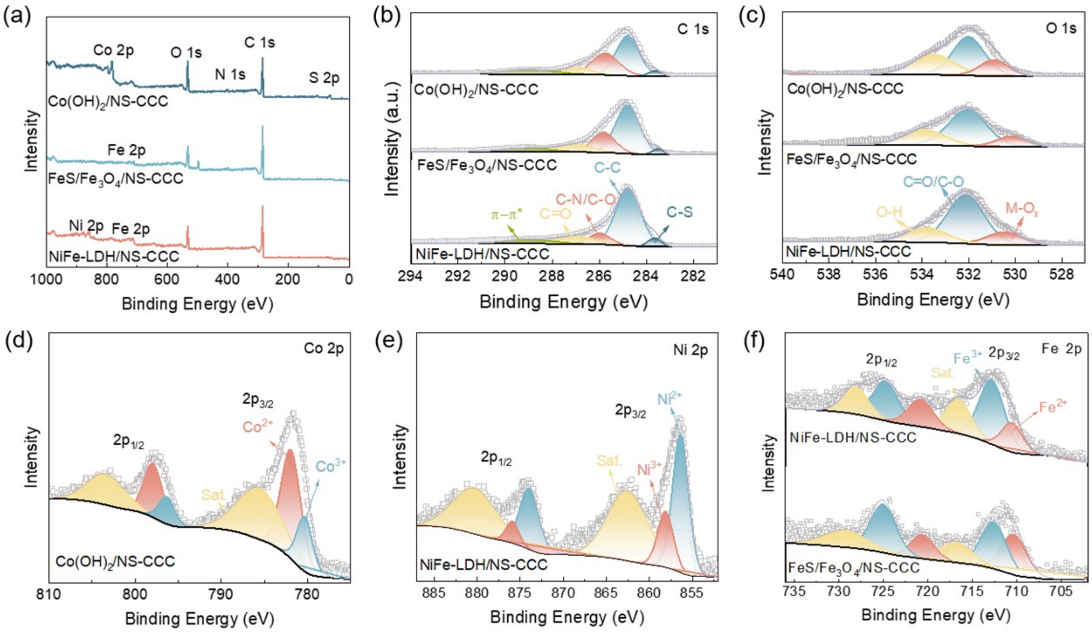

Fig. S12. (a) XPS survey, (b) C 1s, (c) O 1s, (d) Co 2p, (e) Ni 2p, and (f) Fe 2p of the prepared samples.

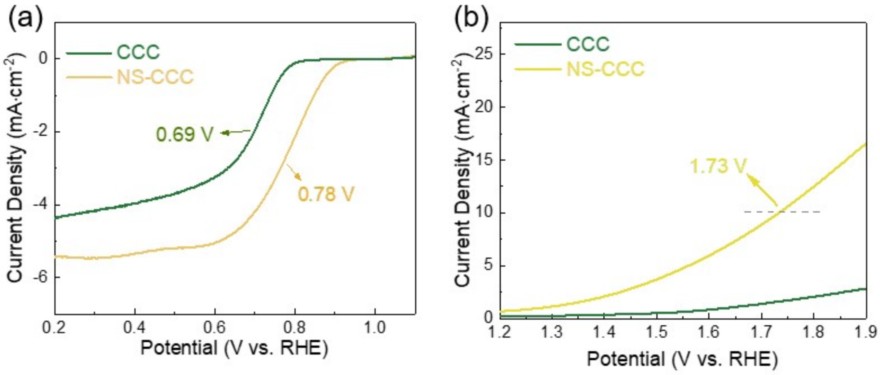

Fig. S13. (a) ORR and (b) OER LSV curves of CCC and NS-CCC.

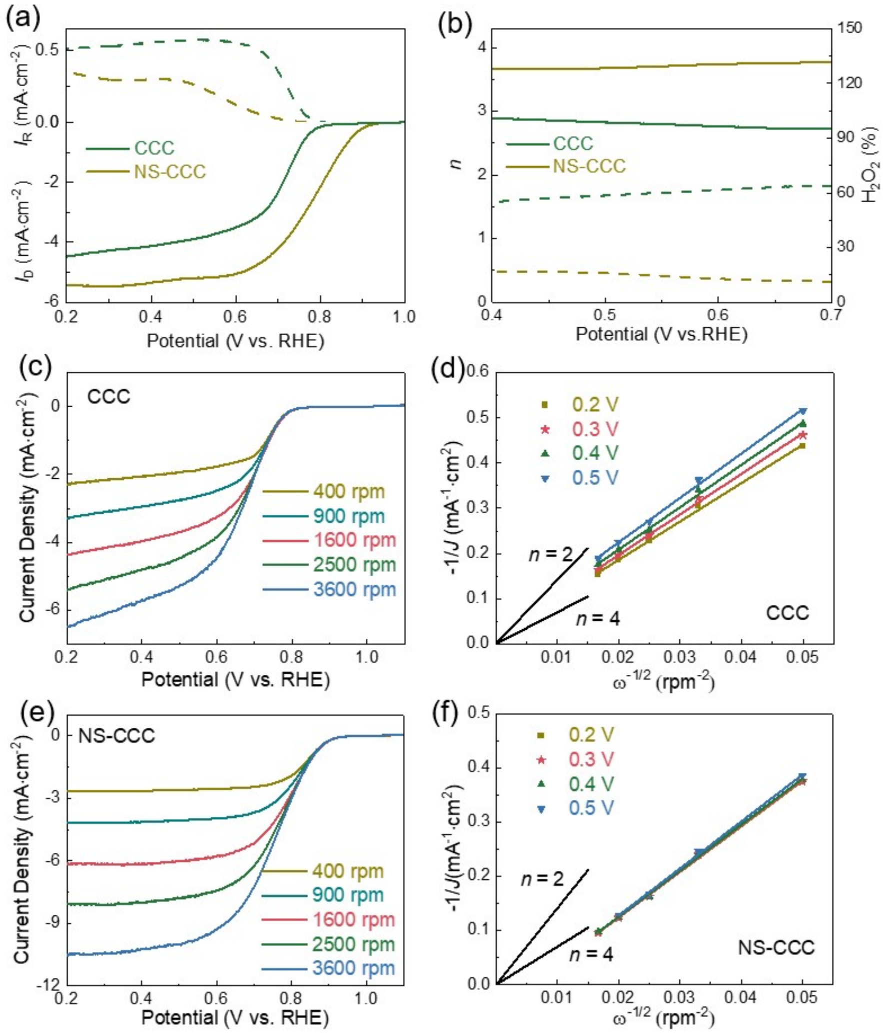

Fig. S14. (a) ORR LSVs with Disk (I_D) and ring (I_R) current density and (b) the corresponding calculated electron transfer number (*n*) and peroxide yield (% H_2O_2) based on the corresponding RRDE data of CCC and NS-CCC. ORR LSVs at different rotating speeds and corresponding K-L plots of (c,d) CCC and (e,f) NS-CCC.

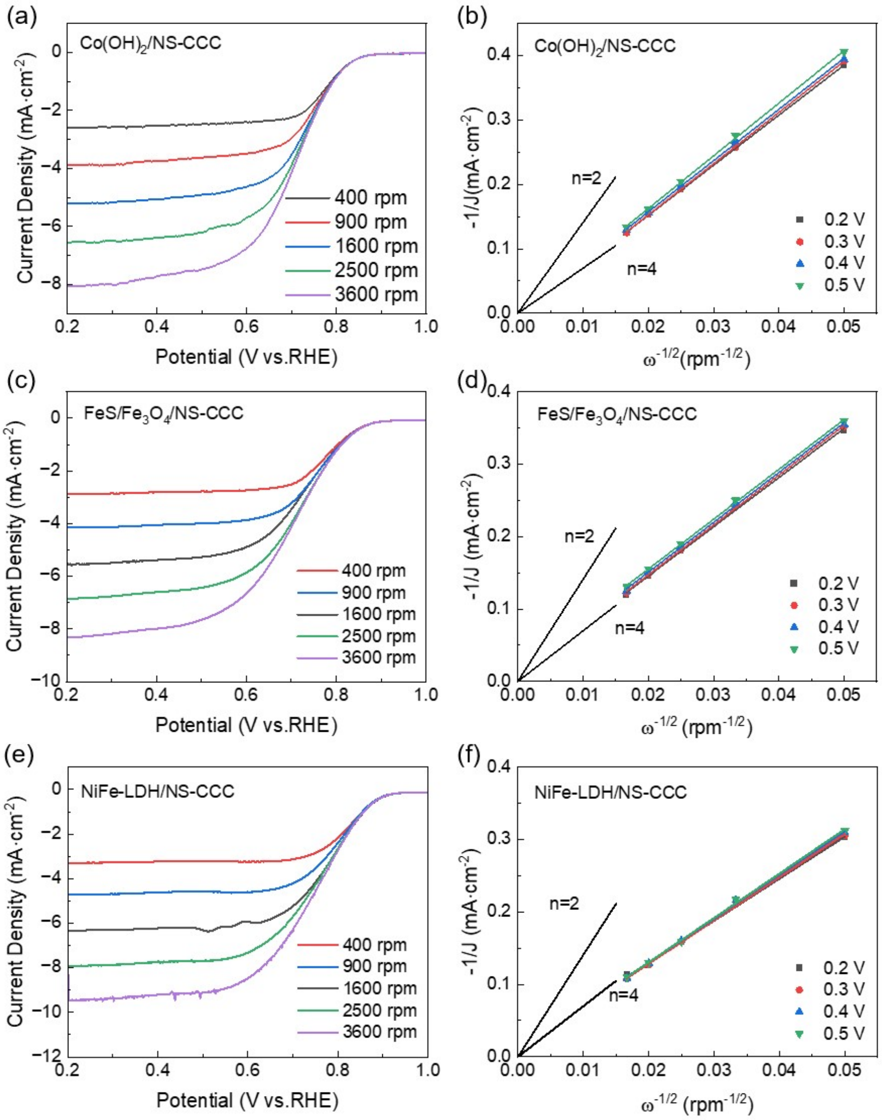

Fig. S15. ORR LSVs at different rotating speeds and corresponding K-L plots of (a,b) $Co(OH)_2$/NS-CCC, (c,d) FeS/Fe_3O_4/NS-CCC, and (e,f) NiFe-LDH/NS-CCC.

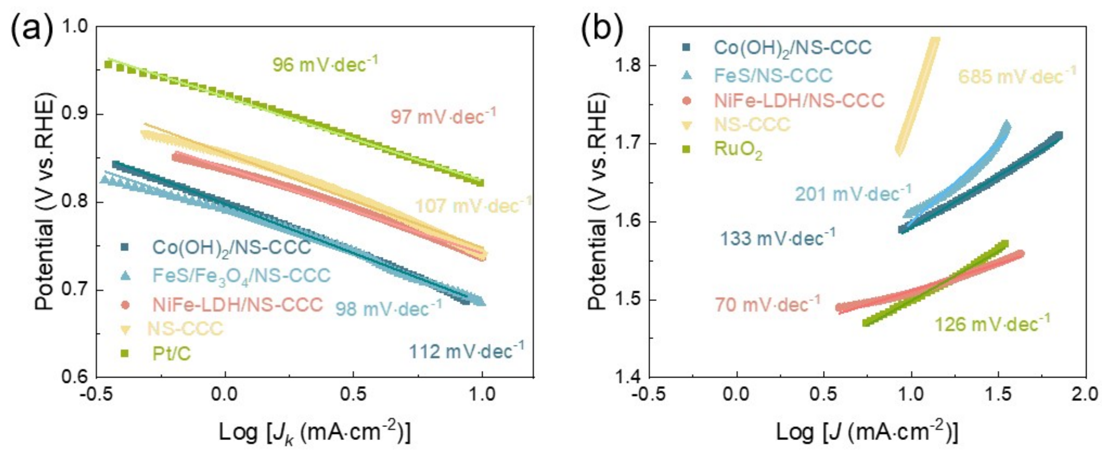

Fig. S16. (a) ORR and (b) OER Tafel slopes of samples.

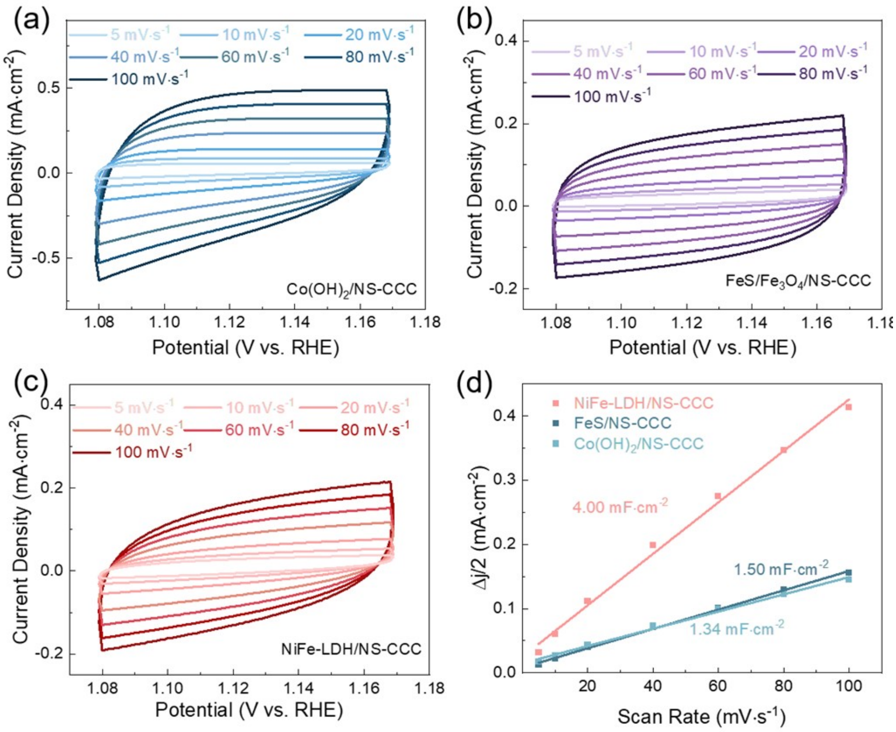

Fig. S17. CV curves with different scanning speeds and fitted lines for C_{dl} of samples.

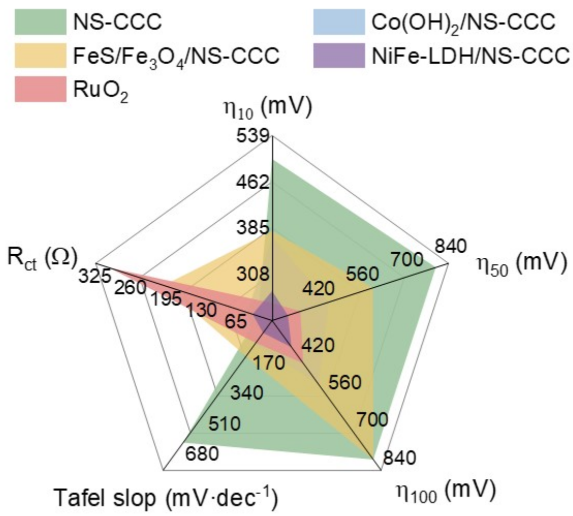

Fig. S18. Overall performance comparison of samples.

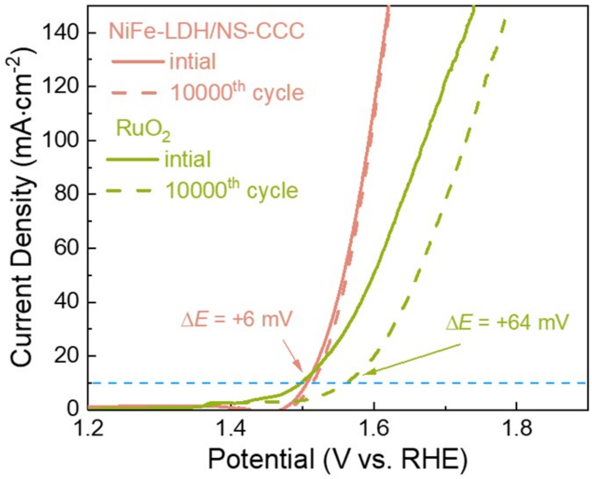

Fig. S19. ADT with LSV curves before and after 10000 cycles of samples.

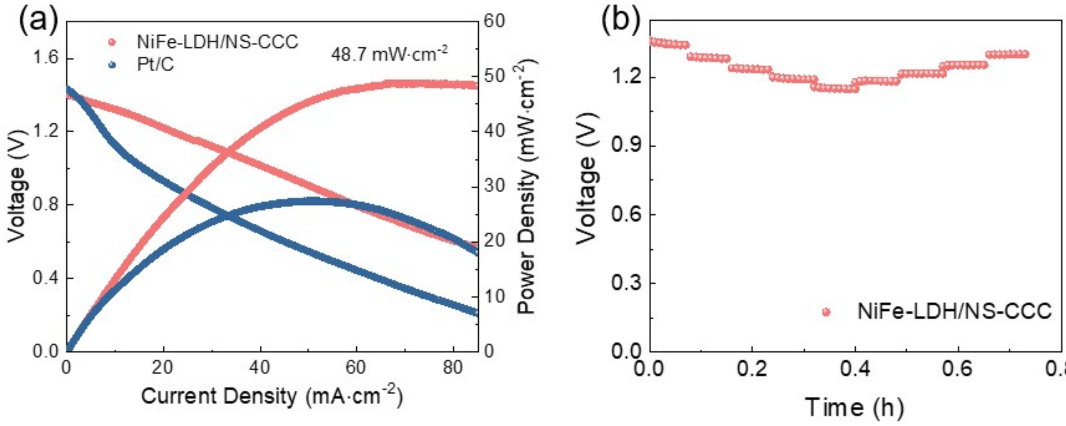

Fig. S20. (a) Discharge polarization/power density curves and (b) rate performances of flexile ZABs.

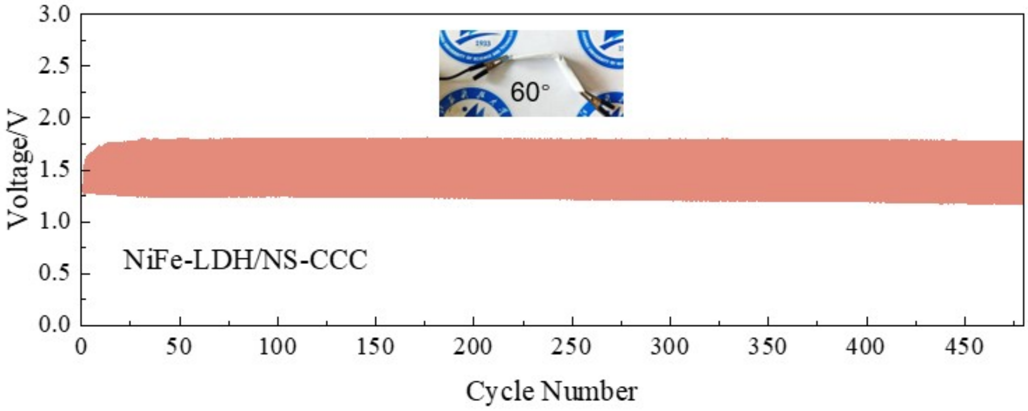

Figure S21. Galvanostatic charge/discharge cycles of FZABs under 60° bending angle.

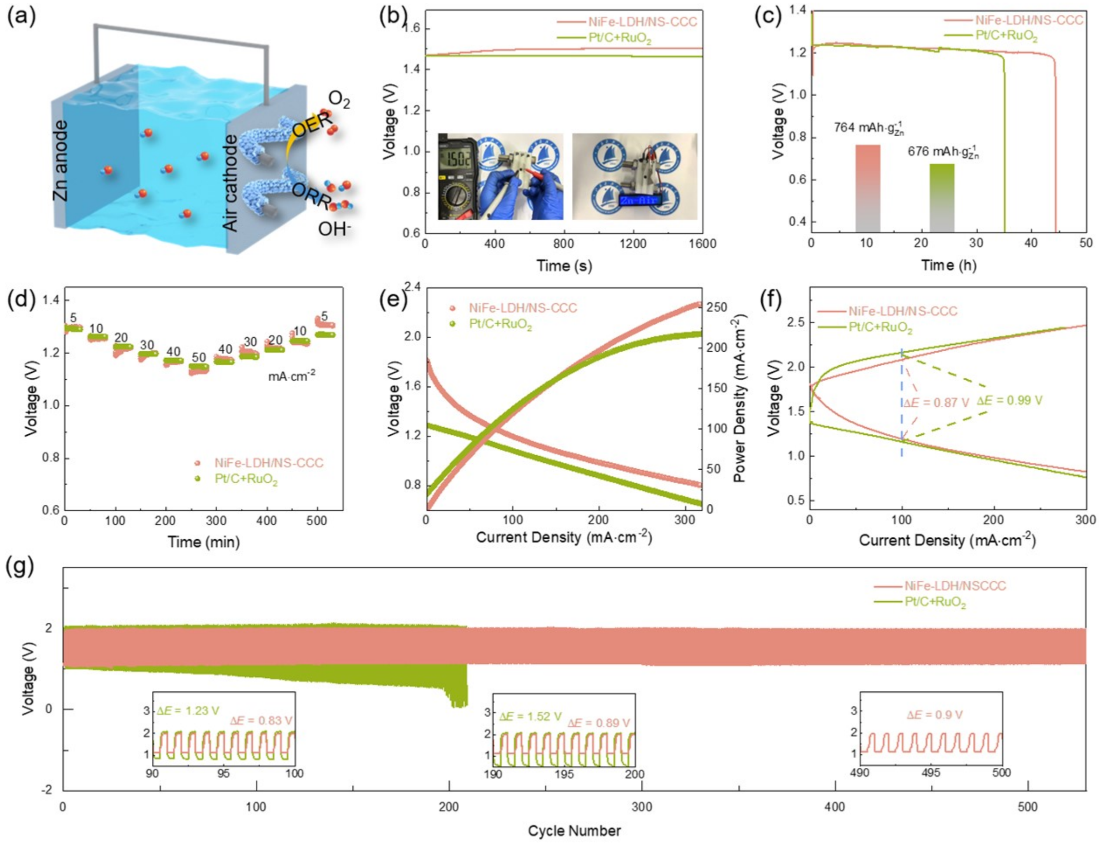

Fig. S22. Liquid ZABs: (a) The schematic illustration, (b) OCV plots (insert are powered multimeter and LED), (c) galvanostatic discharge curves and specific capacities, (d) rate performances, (e) discharge polarization and power density curves, (f) discharge and charge polarization curves, (g) galvanostatic charge/discharge cycles at 10 mA·cm^{-2}.

To evaluate the practical applicability of the bifunctional catalysts in energy storage devices, rechargeable liquid ZABs were assembled using NiFe-LDH/NS-CCC as the optimal ORR/OER catalyst for air cathode, a zinc foil anode, and an aqueous electrolyte containing 6 mol L^{-1} KOH and 0.2 mol L^{-1} $Zn(CH_3COO)_2$ (**Fig. 22a**). Reference batteries employing Pt/C+RuO_2 catalysts were fabricated for benchmarking discharge performance and cycling stability. The NiFe-LDH/NS-CCC-based ZAB achieves a superior open-circuit voltage (OCV) of 1.50 V (**Fig. 22b**), exceeding the Pt/C+RuO_2-based system (1.47 V) and successfully powering an LED (inset, **Fig. 22b**). At 10 mA cm^{-2}, the NiFe-LDH/NS-CCC-based ZAB delivers a high specific capacity of 764 mAh $g^{-1}{}_{Zn}$ (**Fig. 22c**), outperforming the Pt/C+RuO_2 counterpart (676 mAh $g^{-1}{}_{Zn}$). Rate capability tests (**Fig. 22d**) reveals comparable discharge plateaus to Pt/C+RuO_2 across 5–50 mA cm^{-2}, with enhanced voltage recovery during current step-down, demonstrating superior rate tolerance. A maximum power density of 256 mW cm^{-2} at 320 mA cm^{-2} is attained by the NiFe-LDH/NS-CCC-based ZAB (**Fig. 22e**), substantially surpassing Pt/C+RuO_2 (218 mW cm^{-2}). Charge-discharge polarization curves (**Fig. 22f**) exhibit a reduced voltage gap of 0.87 V at 100 mA cm^{-2} for NiFe-LDH/NS-CCC-based ZAB versus the Pt/C+RuO_2 hybrid (0.99 V). Crucially, galvanostatic cycling at 10 mA cm^{-2} (**Fig. 22g**) demonstrates exceptional stability: the NiFe-LDH/NS-CCC-based ZAB maintains a negligible voltage gap variation (0.83–0.90 V) over 500 cycles, whereas Pt/C+RuO_2 exhibits significant degradation (1.23–1.52 V) after just 200 cycles. These results collectively validate NiFe-LDH/NS-CCC as a high-performance bifunctional catalyst for liquid ZABs, offering excellent discharge capacity and cycling robustness.

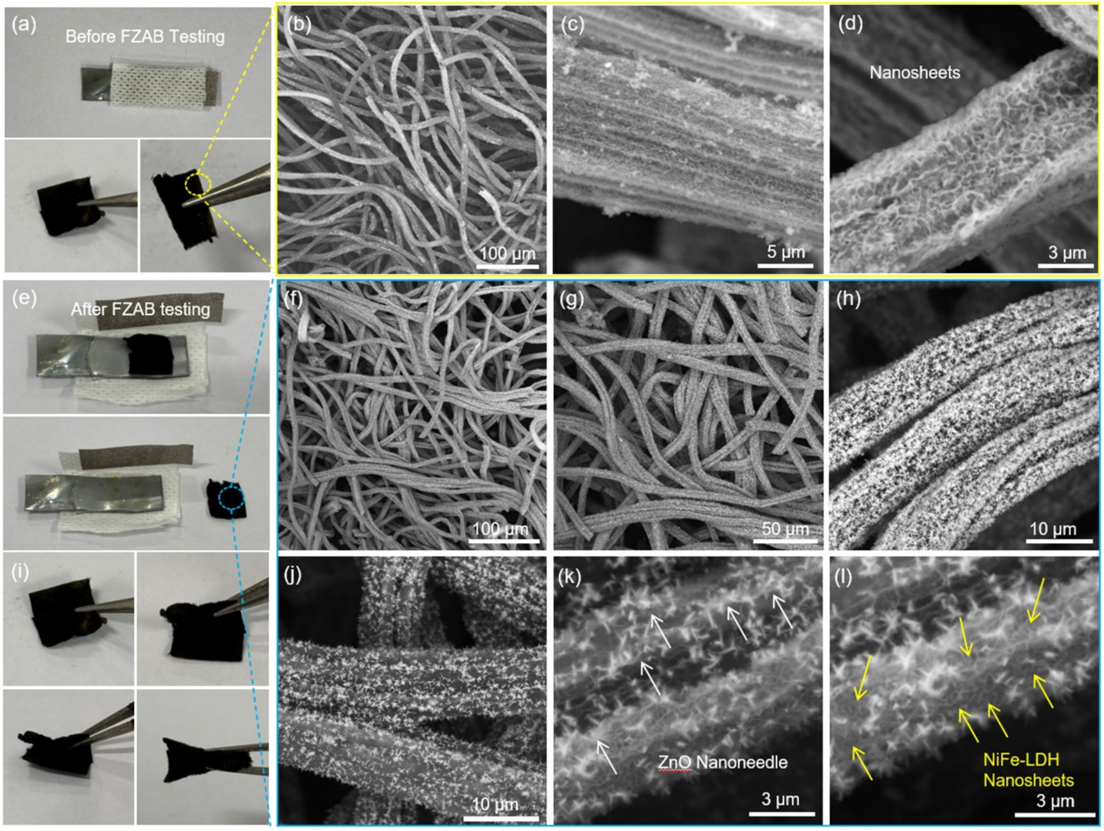

Fig. S23 Photographs and SEM images of NiFe-LDH/NS-CCC electrode (a-d) before and (e-l) after FZAB cycles.

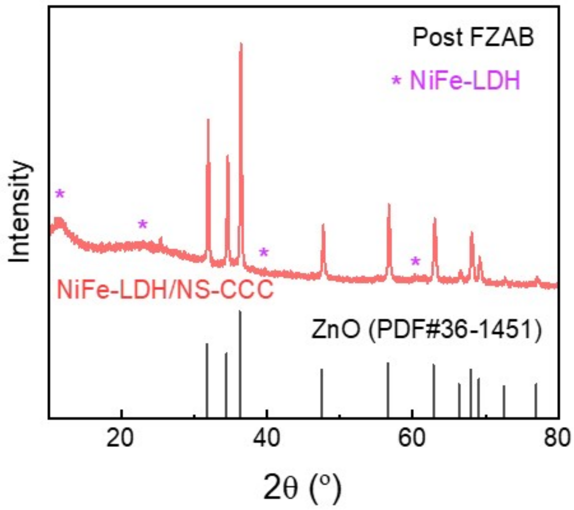

Fig. S24. XRD patterns with PDF cards of NiFe-LDH/NS-CCC electrode after FZAB cycles.

Table S1. Relative atomic contents based on XPS survey of samples.

Samples	C (at%)	O (at%)	N (at%)	S (at%)	Fe (at%)	Co (at%)	Ni (at%)
NiFe-LDH/NS-CCC	73.7	16.5	1.7	1.6	3.0	-	3.5
FeS/Fe_3O_4/NS-CCC	76.1	17.2	2.3	2.0	2.4	-	-
$Co(OH)_2$/NS-CCC	66.9	24.1	1.1	1.4	-	6.5	-

Table S2. ORR and OER activity comparison of recently reported bifunctional catalysts and NiFe-LDH/NS-CCC.

Samples	**$E_{1/2}$ (V vs. RHE)**	**η_{10} (mV)**	**ΔE (V)**	**References**
NiFe-LDH/NS-CCC	0.78	280	0.73	This work
NS-CCC	0.78	500	0.95	This work
CoNi@NCNTs/CC	0.82	330	0.74	[S1]
CoNC@NCXS	0.78	360	0.81	[S2]
FeCo-1/NSC	0.82	330	0.74	[S3]
NiCo-NC	0.86	410	0.78	[S4]
Co_3Ni_1-N–C	0.81	360	0.78	[S5]
FeCo/Se-CNT	0.9	420	0.75	[S6]
Fe_3Co-NC@900	0.88	340	0.69	[S7]
Fe-N-C/NCNT	0.86	442	0.81	[S8]
NSCA/FeCo	0.85	340	0.72	[S9]
$FeCu_{0.3}$-N/C	0.87	410	0.78	[S10]
CoFe@N-CNWF	0.80	320	0.75	[S11]
M-Fe-NCNS	0.88	410	0.76	[S12]
Fe-N-C/N-OMC	0.93	530	0.83	[S13]
Fe-TCNQ-CI	0.96	530	0.82	[S14]
N-Mo-holey	0.85	420	0.80	[S15]
IOSHs-NSC-Co_9S_8	0.82	410	0.82	[S16]
CoXNi-N/C	0.84	360	0.75	[S17]
CoNi-SAs/NC	0.76	340	0.81	[S18]
$Ni-N_4$/GHSs/$Fe-N_4$	0.83	390	0.79	[S19]

Table S3. Impedance fitting values and errors of samples.

Samples	**Rs (Ω)**	**Err%**	**Rc (Ω)**	**Err%**	**Rct (Ω)**	**Err%**
NS-CCC	8.6	0.3	20	1.9	37	1.3
$Co(OH)_2$/NS-CCC	9.5	0.3	79	1.7	46	2.8
FeS/Fe_3O_4/NS-CCC	9.1	0.4	52	1.8	297	3.2
NiFe-LDH/NS-CCC	9.5	0.4	21	1.9	40	1.4

EIS further elucidate reaction kinetics. NS-CCC exhibits minimal catalyst resistance (R_c = 20 Ω) and charge-transfer resistance (R_{ct} = 37 Ω) (**Fig. 3f**), attributable to rapid electron conduction through carbon fibers and interfacial charge transfer via its 3D conductive matrix. NiFe-LDH/NS-CCC (R_c/R_{ct} = 21/40 Ω) and $Co(OH)_2$/NS-CCC (79/46 Ω) retains low resistances, indicating preserved conductive pathways despite OER-phase deposition. Conversely, semiconducting/insulating FeS/Fe_3O_4 substantially increased interfacial barriers (52/297 Ω) (**Table. S3**).

Table S4. Liquid ZAB performances of NiFe-LDH/NS-CCC and recently reported related catalysts.

Sample	Power density curves (mW cm^{-2})	Total Cycles and Times (h)	Current density (mA cm^{-2})	Time per Lap (h)	References
NiFe-LDH/NS-CCC	256	520/520	10	1	This work
Co/NCNTs/CC-1	145.3	500/250	10	0.5	[S20]
H-Co/CeO_2@NCBs	179.8	1200/400	10	0.3	[S21]
Co_9S_8/NCNTs/CC-1	162.5	500/250	10	0.5	[S22]
Co/CoSe@MNCF	214.73	800/400	10	0.5	[S23]
Co@N-CNTs/NSs	142.3	421/126	5	0.3	[S24]
Co_{SAs}@NC-920	166	517/155	2	0.3	[S25]
CNT@Co-$CNFF_{50-900}$	230	433/130	2	0.3	[S26]
FeNiN-CF-15	175	1166/350	5	0.3	[S27]
CoNi-NCNT	180	2400/800	5	0.3	[S28]
A-PpazoPorCo/3D-G	240	2970/495	10	0.16	[S29]
FeN_4ClPO	179.6	900/300	5	0.3	[S30]
FeCoP-$FeCo_2O_4$@PNPC	121.6	>600/240	2	0.3	[S31]
Co_{SA-AC}@SNC	174.1	>830/148	10	0.16	[S32]
CoFe/Co-Fe-S	127	1,562/250	50	0.16	[S33]
Mo-Co_2P@PNC	185	420/140	10	0.3	[S34]
$CoMoO_4$@NC-Co	126.1	270/933	5	0.3	[S35]
NiCo-LDH@SOH	149	2,880/480	5	0.16	[S36]

Table S5. Flexible ZAB performances of NiFe-LDH/NS-CCC and recently reported related catalysts.

Sample	Power density curves (mW cm^{-2})	Total Cycles and Times (h)	Current density (mA cm^{-2}) / Time per Lap (min)	References
NiFe-LDH/NS-CCC	48.7	700/70	2/6	This work
Co/NCNTs/CC-1	60.8	18/6	1/20	[S20]
H-Co/CeO_2@NCBs	112.3	420/70	2/10	[S21]
Co_9S_8/NCNTs/CC-1	87.6	24/8	1/20	[S22]
A-PpazoPorCo/3D-G	66	117/19.5	5/10	[S29]
FeCoP-$FeCo_2O_4$@PNPC	55.26	90/27	2/20	[S31]
FeCoNiCuMo HEA	72.0	90/15	5/10	[S37]
Fe_4N@CNF-NH_3	33.7	19.8/3.3	1/10	[S38]
CoFe-NC	30	133/40	1/20	[S39]
Fe/Fe_3C@N-doped C/CC-700	61.4	129/21.5	5/10	[S40]
CoFe/$CoFe_2O_4$-NCS	103.6	324/54	2/10	[S41]
Fe-Ni/CN	76.1	90/15	5/10	[S42]
$CoSe_2$-$FeSe_2$@NC/NHC	61.4	30/5	1/10	[S43]
70%-γ-MnO_2/KC	62.4	60/10	2/10	[S44]

References

[S1] Tian, W.-W., Ren, J.-T., Yuan, Z.-Y. *Applied Catalysis B: Environmental* **2022,** *317*, 121764.

[S2] Jin, H., Lin, D., Zhou, L., Zha, G., Wu, H., Li, S., Xie, H. *Scientific Reports*, **2025**, *15*(1), 3480.

[S3] Chang, S.; Zhang, H.; Zhang, Z., *Journal of Energy Chemistry* **2021,** *56*, 64-71. DOI 10.1016/j.jechem.2020.07.047.

[S4] Wang, F.; Xu, Y.; Wang, Y.; Liang, Z.; Zhang, R.; Wang, Y.; Zhang, H.; Zhang, W.; Cao, R.; Zheng, H., *Chemical Communications* **2021**. *57*(66), 8190-8193.

[S5] Zhao, Q., Bao, L., Wang, H., Dou, D., Cong, Y., Li, C. *Ionics*, **2024,** *30*(8), 4797-4810.

[S6] Zhang, H.; Zhao, M.; Liu, H.; Shi, S.; Wang, Z.; Zhang, B.; Song, L.; Shang, J.; Yang, Y.; Ma, C.; Zheng, L.; Han, Y.; Huang, W., *Nano Letters* **2021,** *21* (5), 2255-2264. DOI 10.1021/acs.nanolett.1c00077.

[S7] Srinivas, K., Yu, H., Chen, Z., Chen, A., Zhu, M. Q., Chen, Y., Yang, C. *Journal of Materials Chemistry A*, **2024,** *12*(27), 16863-16876.

[S8] Sheng, J., Zhu, S., Jia, G., Liu, X., & Li, Y. *Nano Research,* **2021,** 14(12), 4541-4547.

[S9] Zhang, Y.; Zhang, X.; Li, Y.; Wang, J.; Kawi, S.; Zhong, Q., *Nano Research* **2023**. *Nano Research*, *16*(5), 6870-6880.

[S10] Wang, B.; Xu, L.; Liu, G.; Ye, Y.; Quan, Y.; Wang, C.; Wei, W.; Zhu, W.; Xu, C.; Li, H.; Xia, J., *Journal of Alloys and Compounds* **2020,** *826*. DOI 10.1016/j.jallcom.2020.154152.

[S11] Zhou, Q.; Ai, L.; Li, Q.; Hou, S.; Xu, L.; Sun, D.; Pang, H.; Huang, K.; Tang, Y., *Chemical Engineering Journal* **2021,** *417*. DOI 10.1016/j.cej.2020.127895.

[S12] Wang, M.; Ji, H.; Liu, S.; Sun, H.; Liu, J.; Yan, C.; Qian, T., *Chemical Engineering Journal* **2020,** *393*, 124702.

[S13] Han, J.; Bao, H.; Wang, J.-Q.; Zheng, L.; Sun, S.; Wang, Z. L.; Sun, C., *Applied Catalysis B: Environmental* **2021,** *280*, 119411.

[S14] Chen, T.; Wu, J.; Zhu, C.; Liu, Z.; Zhou, W.; Zhu, C.; Guan, C.; Fang, G., *Chemical Engineering Journal* **2021,** *405*, 125956.

[S15] Du, P.; Hu, K.; Lyu, J.; Li, H.; Lin, X.; Xie, G.; Liu, X.; Ito, Y.; Qiu, H.-J., *Applied Catalysis B: Environmental* **2020,** *276*, 119172.

[S16] N. Xu, J. A. Wilson, Y. D. Wang, T. Su, Y. Wei, J. Qiao, X. D. Zhou, Y. Zhang, S. Sun, Appl. Catal. B Environ. **2020**, 272, 118953.

[S17] Z. Li, H. Li, H. Cao, S. Sun, W. Diao, D. Gao, P. Lu, S. Zhang, Z. Guo, M. Li, R. Liu, D. Ren, C. Liu, Y. Zhang, Z. Yang, J. Jiang, G. Zhang, Appl. Catal. B Environ. **2019**, 240, 112–121.

[S18] X. Han, X. Ling, D. Yu, D. Xie, L. Li, S. Peng, C. Zhong, N. Zhao, Y. Deng, W. Hu, Adv. Mater. **2019**, 31, 1905622.

[S19] J. Chen, H. Li, C. Fan, Q. Meng, Y. Tang, X. Tang, G. Fu, T. Ma, Adv. Mater. **2020**, 32, 2003134.

[S20] Q. Wu, J. Jiang, H. Gao, H. Jia, C. Wu, C. Deng, G. Xu, M. Ammar, H. Jiang, L. Zhang. Carbon cloth-based nitrogen-doped carbon nanotube-encapsulated Co nanoparticles as bifunctional oxygen electrocatalysts for flexible Zn-air batteries. *Journal of Materials Science & Technology*, 2026, 255: 65-74.

[S21] M. Liu, Q. Li, X. Xiao, Z. Xu, S. Zhang, K. Lang, B. Jing, B. Zhang, M. Ding, J. Zou, B. Jiang. Constructing Co-O-Ce bridge in Mott-Schottky Co/CeO_2 heterojunctions facilitates oxygen electrocatalysis bifunctionality for rechargeable Zn-air batteries. *Journal of Energy Chemistry*, 2026, 112: 572-583.

[S22] Q. Wu, H. Gao, H. Jiang, T. Zhao, S. Liu, C. Wu, G. Xu, L. Zhang. In-situ nitrogen-doped carbon nanotube-encapsulated Co_9S_8 nanoparticles as self-supporting bifunctional air electrodes for zinc-air batteries. *Journal of Materials Science & Technology*, 2025, 222: 1-10.

[S23] Y. Song, T. Tang, H. Yang, J. Yu, S. Zhang, C. Deng. Co/CoSe heterojunctions embedded in multilevel nitrogen-doped carbon nanofibers for superior oxygen electrocatalysis. *International Journal of Hydrogen Energy*, 2025, 127: 655-664.

[S24] J. Li, T. Lu, Y. Fang, G. Zhou, M. Zhang, H. Pang, J. Yang, Y. Tang, L. Xu. The manipulation of rectifying contact of Co and nitrogen-doped carbon hierarchical superstructures toward high-performance oxygen reduction reaction. Carbon Energy,

2024, 6(9): e529.
[S25] C. Lv, B. Li, Y. Ren, G. Zhang, Z. Lu, L. Li, X. Zhang, X. Yang, X. Yu. A "MOF-plus-MOF" strategy to synthesize Co-N_3C1 single-atom catalyst for rechargeable Zn-air battery. *Chemical Engineering Journal*, 2024, 495: 153670.
[S26] T. Lu, N. Xu, L. Guo, B. Zhou, L. Dai, W. Yang, G. Liu, J. K. Lee, J. Qiao. Constructing "π-π" reinforced bridge carbon nanofibers with highly active Co-N/C@ pyridine N/C@ CNTs sites as free-standing bifunctional oxygen electrodes for Zn-air batteries. *Advanced Fiber Materials*, 2024, 6(4): 1108-1121.
[S27] K. Li, W. Yuan, Y. Bai, X. Wu, X. Zhang, S. Jiang, C. Wang, W. Zhang, Y. Tang. Spider silk inspired ultrafine carbon nanotubes-crosslinked porous carbon fibers for Zn-air batteries. *Applied Surface Science*, 2024, 677: 161089.
[S28] Y. Du, Z. Zhong, Z. Shi, L. Zhou, S. Pan, X. Xu, Y. Liu, D. Xiong, K. Wang. Dual-ligand engineered CoNi alloy/N-doped carbon nanotubes bifunctional ORR/OER electrocatalyst for long-lifespan rechargeable Zn-air batteries. *Journal of Colloid and Interface Science*, 2025, 683: 631-640.
[S29] Y. Zhuang, Y. Sun, L. Wang, P. Sun, J. Wang, P. Zhang, Z. Li. Full conjugated poly (1, 4-phenyldiazo porphyrin cobalt) covalent organic framework with D-π-A structure enhancing bifunctional oxygen catalytic performance. *Journal of Energy Chemistry*, 2025, 104: 214-224.
[S30] Z. Chen, T. C. Yang, C. M. Yang, C. Bao, Z. Jiang, S. Deng, N. C. Lai. Symmetry distortion engineering single-atom catalysts: Exceptional ORR activity and ultra-stable Zn-air batteries. *Chemical Engineering Journal*, 2025, 516: 164156.
[S31] R. Qi, Y. Shi, W. Tang, T. Liu, L. Gao, K. Tang, R. Liu. Bimetallic phosphides-oxides heterostructures coupled heteroatom-doped carbon as bifunctional electrocatalysts for Zn-air batteries. *Nano Research Energy*, 2025, 4(2): e9120151.
[S32] J. Rong, W. Chen, E. Gao, J. Wu, H. Ao, X. Zheng, Y. Zhang, Z. Li, M. Kim, Y. Yamauchi, C. Wang. Design of Atomically Dispersed CoN_4 Sites and Co Clusters for Synergistically Enhanced Oxygen Reduction Electrocatalysis. *Small*, 20(42): 2402323.
[S33] Y. Deng, T. Liu, L. Lv, M. Fan, G. Ma, X. Yang, Z. Li, D. Yan, G. Ma, H. Wang, H. Wan, C. Wang, H. Wang. An elaborate electron spin modulator of schottky

catalyst for stable alkaline Zn-air battery application. *Journal of Power Sources*, 2025, 631: 236273.

[S34] J. Han, J. Zhou, W. Song, H. Zhang, Z. Wang, K. Liu, Y. Li, W. Zhu, X. Sun, H. Liang. Constructing electron-enriched Co tetrahedral sites to promote oxygen electrocatalysis in rechargeable zinc-air batteries. *Applied Catalysis B: Environment and Energy*, 2024, 359: 124468.

[S35] Q. Feng, H. Kang, Y. Xiao, B. Su, Z. Lei. Bifunctionality of $CoMoO_4$ nanorods with Co, N co-doped carbon heterostructures can be used in zinc-air batteries. *Journal of Energy Storage*, 2025, 122: 116740.

[S36] S. Song, Y. Liu, X. Wang, H. Zhao, J. Ren, W. Ye, J. Ma, R. Ma. S-doped NiCo layered double hydroxides enable efficient and durable methanol oxidation and oxygen reduction reactions for Zn-methanol-air batteries. *Electrochimica Acta*, 2024, 489: 144226.

[S37] T. Y. Lin, F. Y. Yen, Y. C. Ting, P. W. Chen, S. Y. Lu. Non-precious bifunctional high entropy alloy catalyst and layered double hydroxide enhanced gel electrolyte based rechargeable flexible zinc-air batteries. *Chemical Engineering Journal*, 2024, 488: 151093.

[S38] C. X. Xu, J. J. Zhang, H. R. Dou, Y. Z. Li, D. M. Li, Y. J. Zhang, B. Liu, P. Inbaraj, P. P. Huo. Fe_4N particles embedded in nitrogen-doped electrospun carbon nanofibers as efficient ORR catalysts for zinc-air battery. *Rare Metals*, 2025, 44(5): 3156-3169.

[S39] J. Dai, P. Chen, F. Meng, F. Han, C. Zhu, X. Wei, L. Zheng, J. Liu. Starch-reinforced adhesive hydrogel electrolyte enables high-performance flexible zinc-air batteries. *Journal of Energy Storage*, 2024, 102: 114035.

[S40] Z. Wang, J. Ren, G. Ling, J. Guo, Y. Lv, R. P. Ren. Prussian Blue-Derived Atomic Fe/Fe_3C@ N-Doped C Catalysts Supported by Carbon Cloth as Integrated Air Cathode for Flexible Zn-Air Batteries. *Advanced Science*, 2025, 12(1): 2407631.

[S41] S. Chen, J. Zhong, Y. Zhang, Z. Zeng, X. Fang, D. Yuan. Efficient electrocatalysts for zinc-air batteries featuring CoFe/$CoFe_2O_4$ heterojunctions in a nitrogen-doped carbon framework. *International Journal of Hydrogen Energy*, 2025, 159: 150580.

[S42] J. Liu, W. Zhang, Y. Zhang, Z. Sun, S. Du, Y. Wang, Z. Li, X. Niu, W. Sun. Fe, Ni, co-doped ZIF-8 derived in situ grown carbon nanotubes as Zinc-air battery cathode for self-powered electrochemical sensing glucose. *Journal of Alloys and Compounds*, 2025, 1020: 179475.

[S43] Y. Luo, Q. Wu, Y. Fu, M. Wen. Durable built-in electric field in $CoSe_2$-$FeSe_2$@NC on N-doped honeycomb carbon for long-term efficient oxygen electrocatalysis toward zinc-air battery. *Chemical Engineering Journal*, 2025, 512: 162739.

[S44] D. Wang, J. Li, Q. Zhuang, J. Luo, G. Cheng, J. Huang, T. Xue, M. Sun, F. Ye, L. Yu. Ball-Milled γ-MnO_2/Ketjenblack composite as an Efficient Electrochemical Catalyst for Zinc-Air Batteries. *Materials Today Energy*, 2025, 53: 101975.